Article:
Booth, SG, Chang, S-Y, Uehara, A et al. (4 more authors) (2017) In situ XAFS Study of Palladium Electrodeposition at the Liquid/Liquid Interface. Electrochimica Acta, 235. pp. 251-261. ISSN 0013-4686

https://doi.org/10.1016/j.electacta.2017.03.059

Title: In situ XAFS Study of Palladium Electrodeposition at the Liquid/Liquid Interface

Author: Samuel G. Booth Sin-Yuen Chang Akihiro Uehara Camille La Fontaine Giannantonio Cibin Sven L.M. Schroeder Robert A.W. Dryfe

PII: S0013-4686(17)30526-1
DOI: http://dx.doi.org/doi:10.1016/j.electacta.2017.03.059
Reference: EA 29093

To appear in: *Electrochimica Acta*

Received date: 12-1-2017
Revised date: 6-3-2017
Accepted date: 7-3-2017

Please cite this article as: S.G. Booth, S.-Y. Chang, A. Uehara, C. La Fontaine, G. Cibin, S.L.M. Schroeder, R.A.W. Dryfe, In situ XAFS Study of Palladium Electrodeposition at the Liquid/Liquid Interface, *Electrochimica Acta* (2017), http://dx.doi.org/10.1016/j.electacta.2017.03.059

In situ XAFS Study of Palladium Electrodeposition at the Liquid/Liquid Interface

Samuel G. Booth,[a] Sin-Yuen Chang,[b] Akihiro Uehara,[c] Camille La Fontaine,[d] Giannantonio Cibin,[b] Sven L. M. Schroeder[b,e] and Robert A. W. Dryfe[a*]

Addresses

[a] School of Chemistry, University of Manchester, Oxford Road, Manchester, M13 9PL, UK

[b] Diamond Light Source Ltd., Didcot, Oxfordshire OX11 0DE, UK

[c] Division of Nuclear Engineering Science, Research Reactor Institute, Kyoto University, Osaka, 590-0494, Japan

[d] Synchrotron Soleil, L'Orme des Merisiers, Saint-Aubin, BP48, 91192, Gif-sur-Yvette, France

[e] School of Chemical and Process Engineering, University of Leeds, Leeds LS2 9JT, UK

Corresponding Author Email

robert.dryfe@manchester.ac.uk

Abstract

We report the use of XAFS (X-ray absorption fine structure) as an in situ method to follow the electrochemically driven deposition of palladium nanoparticles at a liquid/liquid interface. A novel glass/plastic hybrid electrochemical cell was used to enable control of the potential applied to the liquid/liquid interface. In situ measurements indicate that the nucleation of metallic nanoparticles can be triggered through chronoamperometry or cyclic voltammetry.

In contrast to spontaneous nucleation at the liquid/liquid interface, whereby fluctuations in Pd oxidation state and concentration are observed, under a fixed interfacial potential the growth process occurs at a steady rate leading to a build-up of palladium at the interface. Raman spectroscopy of the deposit suggests that the organic electrolyte binds directly to the surface of the deposited nanoparticles. It was found that the introduction of citric acid results in the formation of spherical nanoparticles at the interface.

Keywords (up to 5)

Palladium, electrodeposition, XANES, nanoparticles

1. Introduction

The synthesis of metallic nanoparticles has been a focus of researchers in numerous fields due to their potential applications in energy conversion, catalysis and therapeutics amongst others. Widely developed synthetic strategies to effectively form nanoparticles with precise control of the shape and size have been developed, such as the Turkevich or Lee-Meisel methods to produce citrate protected nanoparticles (20-50 nm) and the Brust-Schiffrin method to form smaller (1-5 nm), thiol protected particles [1-3]. In order to further develop the synthetic strategies to form nanoparticles with precisely controlled size, shape and composition, a clear understanding of the nucleation and growth processes involved is required. As an addendum to this there is also a desire to develop fine control strategies to form the target structures as efficiently as possible.

Whilst a variety of approaches to probe solution phase nucleation have been reported in the literature over the past decades, many aspects of the process are relatively poorly understood. The size domain of the critical first stages of nucleation, which is believed to be on the order

of nanometres or sub-nanometres, has proven difficult to verify both experimentally and computationally [4-6]. Experimentally, detection of species on this scale is very difficult without the high sensitivity (spatial and temporal) instrumentation capable of sampling at the right scale and differentiating the nucleation events from the bulk species. Computationally the sizes of system required to effectively model the events are quite large, making calculations very expensive.

Due to the development of ever more precise experimental techniques however, the size domains of interest are now becoming accessible. Techniques such as transmission electron microscopy (TEM), X-ray scattering and X-ray absorption spectroscopy may now provide incisive information about the phase changes. In particular coupled in situ techniques such as UV-Vis absorbance and X-ray scattering can enable clear resolution of the changes occurring during a single phase growth process [7, 8]. The complementary benefits of in situ X-ray techniques to different sections of the nucleation process have been summarised in the review by Sun and Ren [9].

In situ XAFS (X-ray absorption fine structure) can be applied to provide information about the earliest stages in the nucleation process such as changes in the oxidation state of the metal and coordination environment. The technique has been adapted to follow the Turkevich and Brust-Schiffrin methods mentioned above, and other single phase reduction protocols [10-13].

Alongside the aforementioned size based limitations, the study of nucleation is also complicated by a difficulty in defining both the locus and the onset of the reaction. When examining a bulk, supersaturated solution the onset of nucleation is stochastic. The first

nucleation event often triggers a cascade whereby particle nucleation and growth spread rapidly through the whole solution. Pre-nucleation clusters have also been seen to form in undersaturated solutions as well as supersaturated solutions [14], but as the time and location of the initial event is unknown, detection is extremely challenging.

In this respect, when looking to follow the nucleation process, electrochemical systems offer a significant advantage over chemical reactions. By applying an external potential bias to drive the reaction the onset of nucleation can be defined in time and confined in space. As a surface sensitive technique, electrochemistry also delivers control over the location of the reaction whilst enabling direct measurement of the underlying thermodynamics and kinetics. In situ microscopic methods such as atomic force microscopy (AFM) or liquid-phase TEM can be utilised to follow the growth process [15-18]. The drawback of studying nucleation and growth through electrochemistry on a solid electrode is the presence of defects on the electrode surface which act as preferential nucleation sites causing heterogeneity within the reaction [19]. An alternative is to study the processes occurring at a liquid/liquid interface [20], where the interface between the two immiscible fluid phases provides a defect free substrate to follow the nucleation. The reaction at the liquid/liquid interface is considered analogous to that at a liquid/solid interface, i.e. on a “conventional” electrode surface, in the sense that an electron transfer process results in the formation of a zero valent nucleus, which must rapidly grow to a certain size to become stable. The electrodeposition of a number of metals at the liquid/liquid interface has been reported in the literature including Au, Ag, Pt and Pd [21-28], as reviewed elsewhere [29]. In the case of Au nucleation it has been shown that the lack of defect sites can completely inhibit the nucleation process under certain conditions [30]. So far there has only been limited potential dependent size control reported in liquid/liquid deposition reactions [22].

The “soft” interface means that a number of techniques which are readily applied to solid surface, such as atomic force microscopy, are inapplicable. Liquid-phase TEM, which is far from trivial due to the vacuum requirement, has yet to be developed to deal with the complication of the two solvents required in liquid/liquid reactions. XAFS however, can be applied to study such systems under ambient conditions with relative simplicity [30, 31].

When studying reactions at liquid/liquid interfaces it is important to consider the increased complexity of the reaction. As discussed by Schiffrin and co-workers, the reaction is diffusion limited not only by the metal precursor in the aqueous phase but also by the organic reducing agent [28]. As nanoparticles begin to nucleate at the interface there are two factors driving the preferential forward reaction: first, the formation of a lower energy interface e.g. the total surface energy of the system may be reduced as the sum of the organic|solid and aqueous|solid phase interactions are lower in energy than the organic|aqueous interaction [32, 33]. Second, there is the increased likelihood of reactant interaction – initially the reactants must come in to direct contact at the interface for the electron transfer process to occur, but as the particle begins to grow there is an increased reaction cross-section, as further electron transfer processes can occur between reactants present anywhere on the surface. Therefore the particles can be considered as miniature solid bipolar electrodes adsorbed at the interface [28]. Whilst these two processes contribute to the driving force for the forward reaction, the rate may become restricted by the formation of a reactant depletion zone around the newly formed metal structure, which leads to either diffusion limited growth or the dissolution of unstable clusters. If nuclei fail to reach a critical size they may be prone to dissolution [34, 35]. Oscillatory deposition or dissolution processes have previously been observed in electrochemical systems where one parameter (potential/current/resistance) is free to vary

during the reaction [36, 37]. Likewise in chemical systems, the reversible formation of metastable pre-nucleation clusters have been observed previously by XAFS and TEM [38-40].

In this work we focus on the introduction of electrochemical control to the previously reported reduction of Pd^{2+} by ferrocene (Fc) [40-43]. The reaction required an aqueous phase palladium salt ($[PdCl_4]^{2-}$) brought in to contact with a solution of the reducing agent (Fc) in trifluorotoluene (TFT). This resulted in the interfacial reaction forming palladium nanoparticles [42]. Equation 1 indicates the process involved, where *aq* refers to the aqueous phase, *org* the organic phase, and *i* the liquid/liquid interface.

$$[PdCl_4]^{2-}{}_{aq} + 2\ Fc_{org} \rightleftharpoons Pd^0{}_i + 2\ Fc^+{}_{org} + 4\ Cl^-{}_{aq} \quad (1)$$

During deposition, in the absence of potential control, there are significant fluctuations in both interfacial concentration and oxidation state of the Pd, suggesting random oscillations between reduction and dissolution prior to the formation of stable Pd clusters. These oscillations are mimicked by the interfacial potential which is found to vary significantly when not controlled [40]. The presence of a common ion to fix the interfacial potential appeared to suppress the observed oscillations [43] as predicted in the review by Koper [37]. This work uses an external potential bias to exhibit greater control over the growth process in order to identify differences between the potentiostatic and spontaneous deposition processes.

2. Experimental

2.1 Chemicals

$(NH_4)_2PdCl_4$ (99.995%), trifluorotoluene (TFT, ≥99%), LiCl (≥99.99%), bis(triphenylphosphoranylidene)ammonium chloride (BTPPACl, ≥98%) and citric acid (≥99.5%) were purchased from Sigma-Aldrich (Dorset, UK). Fc (98%) and sodium tetrakis[3,5-bis(trifluoromethyl)phenyl]borate (NaTFPB, ≥ 97%) were purchased from Alfa Aesar (Lancashire, UK). Ultrapure filtered water (Milli-Q, 18.2 MΩ resistivity) was used in the preparation of all aqueous solutions. The organic electrolyte, BTPPATFPB, was synthesised through metathesis reaction of BTPPACl and NaTFPB in 2:1:1 acetone:ethanol:water mixture as reported previously [44, 45]. All electrochemical cells were cleaned in either piranha or aqua regia solutions prior to use.

2.2 Electrochemistry

Two types of electrochemical cell were used to record the data. The first was a standard 4-electrode, glass electrochemical cell, Figure 1(a). For this cell the internal volume is ~4 mL. Luggin capillaries connect the reference solutions to the main cell. In order to perform in situ XAFS measurements we developed a modified plastic cell, Figure 1(b). The main body of this cell was a 2 mL polypropylene Eppendorf safe-lock tube. The cells have been previously used by us in a variety of synchrotron-based XAFS studies of single phase and two-phase systems: no evidence of degradation, due to the presence of the organic solvent, was observed [40, 43, 46]. Two holes were drilled into this tube in order to place glass Luggin capillaries close to the interface. The capillaries were secured in place using an epoxy adhesive (Araldite). For each use the cell had to be acid cleaned removing the epoxy which was then reapplied to the cell to use again. The interfacial area of the polypropylene is similar to that of the glass cell, although there is a larger distance between the Luggin capillaries and the interface, because the glass capillaries would otherwise interfere with the passage of the X-ray beam.

Figure 1

In both cases a 4-electrode set up was applied using Pt gauze electrodes as counter electrodes and homemade Ag/AgCl reference electrodes for both the aqueous and organic phases. The organic reference required the use of an aqueous reference solution containing 1 mM BTPPACl and 10 mM LiCl. For reactions in the home lab and at the synchrotron the concentrations used were: *x* mM $PdCl_4^{2-}$ (*x* = 1, 5 or 10) and 0.1 M LiCl in the aqueous phase, and *y* mM Fc (*y* = 4, 5, 10 or 20) and 10 mM BTPPATFPB in the organic phase.

Home-lab electrochemical measurements were conducted on an Autolab PGSTAT100 (Metrohm, Runcorn, UK). In situ measurements during beamtime experiments were performed using an Ivium Compactstat potentiostat (Ivium Technologies, Eindhoven, NL). All reported potentials are on an Ag/AgCl scale as recorded.

2.3 XAFS Measurements

In situ experiments were conducted at the quick EXAFS (QEXAFS) beamlines – B18 [47] at the Diamond Light Source and ROCK [48] at Synchrotron SOLEIL, and on the energy dispersive EXAFS beamline ODE [49] at Synchrotron SOLEIL. Pd K-edge measurements were collected at different heights intersecting the liquid/liquid interface during the course of the reaction. In each case we used a beamline script to enable us to repeatedly cycle through a series of positions normal to the interface in order to follow the reaction. Due to the meniscus of the interface there are several positions at which we can see variations during the course of the reaction. The point of greatest interest as far as the reaction is concerned is the point closest to the organic bulk phase. However, at this position we have the lowest Pd K-edge

step height. On ROCK at SOLEIL the signal was sampled for different periods of time at the different heights to counteract this loss of signal.

The synchrotron at SOLEIL ran with an energy of 2.75 GeV. ROCK provided measurements using a Si(220) crystal monochromator oscillating with a frequency of 0.5 Hz over a range of 0.5° to record the complete Pd EXAFS spectrum. Only the increasing angle spectra were considered, resulting in the collection of a complete EXAFS spectrum in 1 s every 2 s. Both fluorescence and transmission spectra were collected simultaneously using, respectively, a passivated implanted planar silicon detector (PIPS, Canberra) and ionization chambers (Oken). The spectra were subsequently averaged to gather data with a suitable signal to noise ratio. It was necessary to average over a greater number of scans when sampling closer to the bottom of the interfacial meniscus. As such, 86 spectra were averaged at the highest sampling position when closer to the aqueous phase, and 144 spectra when at the two positions which intersected more of the organic phase. The beam size was 250 μm (height) × 345 μm (width). On ODE a bent single crystal silicon (311) crystal provides a polychromatic beam that is focused on the sample giving a spot size of 50 μm (height) × 200 μm (width). The transmitted beam then diverges on to a position sensitive Princeton Applied Research Pixis 400 CCD camera. Measurements took 250 ms and were averaged over 100 scans resulting in 25 s per measurement. The presence of a Pd mirror within the ODE optics set up resulted in a minor distortion of the Pd K-edge response.

At the Diamond Light Source, the storage ring runs with an energy of 3 GeV and a current of 300 mA. On the B18 beamline, the beam dimensions were 100 μm (height) × 1000 μm (width). Fluorescence data was collected using a 9-element Ge solid state detector. In this case each measurement took ~3.5 minutes. The beam sizes specified above define the spatial resolution of the experiments: the particles initially formed are on the scale of a few

nanometres in diameter (*section 3.3*), hence each XAFS experiment represents an average of spectra over many individual particles.

Data analysis was performed using the Demeter software package [50]. Initially all spectra were calibrated to a Pd foil sample collected concurrently with each data point, the peak of the first derivative in this spectrum was then calibrated to the known Pd K-edge energy of 24 350 eV. XANES (X-ray absorption near edge structure) data was normalised and treated using the Athena package. Linear combination fitting (LCF) was performed using a standard for $[PdCl_4]^{2-}$ which was collected in the bulk aqueous phase in the absence of reducing agent and Pd foil as the standard for Pd(0), or the initial and final spectra collected during a reaction. The data was fitted between 20 eV below the onset of the K-edge (designated E_0) to a position 200 eV above the edge.

2.4 TEM

TEM micrographs were collected on a Philips CM20 TEM. The samples were collected on copper mesh holey carbon grids purchased from Agar Scientific (Agar Scientific Ltd. Essex, UK). The holey carbon grid was passed through the liquid/liquid interface in order to collect the metal nanoparticles before washing with ethanol and acetone to remove organic salt and solvent residues from the surface.

2.5 Raman

The Raman spectra were recorded on an inVia microscope (Renishaw plc., Wooton-Under-Edge, UK) using a 532 nm laser excitation. A 90° adapter was attached to the objective lens in order to gather spectra in the plane of the liquid/liquid interface.

3. Results and Discussion

3.1 Cyclic voltammetry

The electrochemical deposition of Pd at the liquid/liquid interface is reliant on the application of potential in order to drive the heterogeneous electron transfer process between $Pd^{2+}_{(aq)}$ and $Fc_{(org)}$ (Figure 2) [28, 41].

Figure 2

The reduction potential for $[PdCl_4]^{2-}_{(aq)}$ to Pd^0 has been reported as 0.39 V vs Ag/AgCl in aqueous solution [51], however the actual potential is also a function of the chloride ion concentration [52].

In our studies no deposition was detected without the application of an overpotential to "trigger" the nucleation of Pd metal at the interface. This may be related to the relatively low concentrations used in the present work. In previous work the reaction has been found to occur spontaneously at higher reactant concentration [40, 43].

In liquid/liquid electrochemical systems, the width of the potential window is limited by the transfer of the background electrolyte. Using the very hydrophobic organic electrolyte BTPPATFPB the window is limited by the transfer of Li^+ at the positive end of the potential window and by Cl^- transfer at the negative end [53]. Voltammetry indicates that the onset of Pd nucleation is detectable within this potential window (Figure 3). During the first cycle there is a minor peak visible for the transfer of the ferricenium ion, Fc^+ ($\Delta^{Aq}_{TFT}\phi^o$ 0.51 V) present prior to the onset of the reduction. The small positive peak that is visible in the first scan is due to the photooxidation of a small quantity of ferrocene in the organic phase as reported elsewhere [54, 55]. On cycling beyond the Fc^+ ion transfer peak to more positive

potentials, a hysteresis loop is observed indicative of palladium nucleation [56, 57]. During the second cycle there is an increased peak current for the Fc^+ that has been generated by the reduction of Pd. Repeat cycling indicates further growth as the irreversible peak at the positive end of the potential window continues to increase in current as does the Fc^+ transfer peak until a plateau is observed. The rising current at the right of the CV (0.8 V – 1.0 V) could stem from the electron transfer reaction, but there is also the possibility of overlap with hydrogen evolution catalysed by the Pd^0 already deposited [58].

Figure 3

Current measurements at a fixed potential can provide useful information about the potential dependence of the reaction and the onset of nucleation. Figure 4 indicates the variation in the response at different applied potentials. An initial drop in current is associated with charging of the electrical double layer. In the case of a liquid/liquid system there are two back-to-back electrical double layers extending into the two solvent phases. At a potential above the nucleation threshold (~0.85 V) this is followed by an increase in current until the particle growth becomes limited by mass transport. The results in Figure 4 indicate that the reaction requires a minimum potential of approximately 0.85 V, corresponding to an overpotential for Pd nucleation of approximately 0.46 V, based on the reduction potentials quoted above. The peak in the current response at 0.95 V is probably not observable due to the aforementioned onset of hydrogen evolution, which complicates the current response. Cyclic voltammetry performed directly after applying the fixed potential (Figure 4b) provides more insight into the role of the applied potential. The higher the applied potential, the further the reaction has progressed according to the CV response.

Figure 4(a and b)

If the growth process is thermodynamically favourable then the application of a sufficient overpotential will enable the nucleation clusters to grow through reduction of ions on their surface. Under constant potential the nuclei can form and grow, but the process causes depletion of reactants near the particle/solution interface and a disruption of the local overpotential around the particle. Describing the process involved becomes challenging then as the population of nucleation clusters increases and the diffusion zones between particles start to overlap. One of the most commonly used models to describe this process is that proposed by Scharifker and Hills [18, 59-61]. This model can be used to describe instantaneous nucleation in the limit of an infinite nucleation rate, meaning all nuclei are formed at the initiation of the reaction as in Equations 2 and 3,

$$I = \frac{z\mathrm{F}\mathrm{D}^{1/2}c}{\pi^{1/2}t^{1/2}}\left[1 - \mathrm{e}^{(-N\pi k\mathrm{D}t)}\right] \tag{2}$$

$$k = \left(\frac{8\pi cM}{\rho}\right)^{1/2} \tag{3}$$

where z is the number of electrons transferred, F is the Faraday constant, D is the diffusion coefficient, c is the reactant concentration, N is the nuclei density, M is the molecular weight of the deposit, and ρ is the density of the deposit. If instead progressive nucleation takes place, whereby nuclei are able to form throughout the process, the model may be adapted as in Equations 4 and 5.

$$I = \frac{z\mathrm{F}\mathrm{D}^{1/2}c}{\pi^{1/2}t^{1/2}}\left[1 - \mathrm{e}^{\left(\frac{-AN_0\pi k'\mathrm{D}t^2}{2}\right)}\right] \quad (4)$$

$$k' = \frac{4}{3}\left(\frac{8\pi cM}{\rho}\right)^{1/2} \quad (5)$$

Here, A describes the nucleation rate constant and N_0 is the number of nuclei present initially. The experimental response can be converted to dimensionless variables in order to compare with the theoretical responses. To achieve this, the current is converted to I/I_{Max} where I_{Max} is the peak in the current transient and t/t_{Imax} where t_{Imax} is the time at which the current maximum occurs. The equations for instantaneous and progressive nucleation can then be simplified as shown in Equations 6 and 7, respectively.

$$\left(\frac{I}{I_{\mathrm{Max}}}\right)^2 = \frac{1.9542}{t/t_{\mathrm{Imax}}}\left[1 - \mathrm{e}^{-1.2564\frac{t}{t_{\mathrm{Imax}}}}\right]^2 \quad (6)$$

$$\left(\frac{I}{I_{\mathrm{Max}}}\right)^2 = \frac{1.2254}{t/t_{\mathrm{Imax}}}\left[1 - \mathrm{e}^{-2.3367\frac{t^2}{t_{\mathrm{Imax}}^2}}\right]^2 \quad (7)$$

The current transients measured at 0.85 V and 0.90 V in Figure 4 produced peak maxima in the current transients and can therefore be compared to the model using Equations 6 and 7. When fitted to the model the data adheres more closely to a progressive nucleation response whereby nuclei are able to form throughout the reaction (Figure 5). The fact that the transient response in both cases decreases even more rapidly than the response predicted from the progressive nucleation model is due to the additional complication of diffusion in both the aqueous and the organic phase, as alluded to in the Introduction. Although this problem has

been approached through in depth analytical and numerical studies of electrodeposition at the liquid-liquid interface, a general interfacial growth law has yet to be determined for nucleation at the liquid/liquid interface [28, 62]. As the fit does not closely match the data the results were not used to calculate the diffusion coefficient or nuclei density.

Figure 5(a and b)

3.2 In situ XAFS measurement of palladium deposition

3.2.1 Bulk growth of Pd nanoparticles

Electrochemical measurements were coupled with in situ XAFS in order to obtain information on reactant and product concentrations as well as oxidation state information. This enables measurements with spatial contrast to follow the nucleation and growth process, and to support the mechanistic suggestions made above. In order to perform in situ measurements the electrochemical cell described in Figure 1b was used, as the X-ray beam is strongly attenuated by glass. The meniscus formed between the aqueous and organic phases results in variations in the signal response depending on the vertical sampling position (Figure 6a). The variation in Pd K-edge height (Figure 6b) at the three positions is due to the different concentrations of Pd within the beam as indicated in the schematic in Figure 6a. Due to the interfacial meniscus it is difficult to define the positions relative to the interface, however as an approximation Position A can be considered to be close to the bulk aqueous phase and Position C is close to the bottom of the meniscus. As expected, no Pd could be detected in the organic solution. In this first reaction we depict three positions (vertically separated by 500 µm) which were alternately monitored throughout the reaction in order to demonstrate the spatial dependence of the reaction. For all subsequent examples we show

only the position which gave the clearest response – i.e. the best compromise between signal intensity and proximity to the organic bulk phase.

Initially XAFS measurements were performed over a period of 3.5 h with the interfacial potential held at 0.3 V and then 0.4 V to verify that no reaction occurred at these potentials. As can be seen from the light coloured spectra in Figure 6b, this resulted in minimal variation in the composition of Pd, which also demonstrates that there is no beam induced reaction in this system. In Figure 3 the reaction had plateaued by the sixth CV cycle so in this XAFS experiment, six CV cycles were performed using the same potential window. This resulted in the formation of a visible dark deposit of palladium at the liquid/liquid interface. Following the reaction there was a clear variation in the XAFS response (Figure 6b – red spectra). As would be anticipated, the largest change in Pd concentration is found closest to the organic phase (Position C). The rapid increase in Pd concentration corresponded to a build-up of bulk Pd species at the interface. Linear combination fitting (LCF) yields a fit suggesting 56.9% Pd(II) ($[PdCl_4]^{2-}$) and 43.1% Pd(0) using $[PdCl_4]^{2-}$ and Pd foil as standards (Figure 6c).

Figure 6 (a, b and c)

3.2.2 Progressive Pd growth by restricted CV cycling

In order to follow the process systematically, voltammetry was conducted in a restricted potential window (0.2 – 0.7 V). The positive limit of the potential window was then progressively increased after XAFS measurements at each position (Figure 7a). Between CV cycles the potential was fixed at 0.4 V whilst XAFS spectra were collected. The inset in Figure 7a shows that hysteresis loops, indicative of nucleation, could be observed in three of the CVs collected. The distortion of the CVs at the most positive potentials, compared to

Figure 3, relates to an increase in hydrogen evolution when the reaction is performed over a longer timespan as has been seen in other metal deposition systems [58]. There is also, however, a higher Ohmic drop in the CV shown in Figure 7a, manifest in the wider peak-to-peak separation of the Fc^+ ion transfer discussed earlier. No Ohmic compensation was applied to the experimental voltammograms: the higher distortion seen with the *in situ* XAFS cell reflects the different cell geometry (Figure 1), where the Luggin capillaries are further from the interface (*see section 2.2*). After CV cycling reached the limit of the potential window a fixed potential bias was applied (0.85 V, 120 s) to drive bulk growth of Pd (Figure 7b).

Figure 7 a-d

When examining the XANES response, LCF using Pd foil indicated a slight mismatch between the standard and the nanoparticle product formed at the liquid/liquid interface (Figure S2). With the reaction proceeding directly from Pd(II) to Pd(0) without the formation of any intermediate species (raw spectra in Figure S3) it was possible to use the initial and final spectra from the reaction to examine the deposition process (Figure 7c). Previous reports indicate the rapid formation of poly-nuclear Pd species ($n[Pd(OH)_4]^{2-}$) in aqueous solution which may form precipitates [8]. This reaction can be mitigated at low pH however, in this system this species was not observed suggesting that a high Cl^- content also stabilises the $[PdCl_4]^{2-}$ species as has been confirmed for $[AuCl_4]^-$ [63].

Figure 7d shows example linear combination fits for the data points marked as A and B. Whilst Component 2, the spectrum collected following bulk deposition, still contains some $[PdCl_4]^{2-}$ from the aqueous phase, there is clear variation between the response and that of Pd

foil. The two peaks directly above the edge correspond to transitions to the 5p and 4f states [64]. The reduction in intensity of the second peak in Component 2 relative to the foil indicates a reduction in the density of states as small clusters have been formed rather than bulk metal [65]. The shift to lower energies would appear to suggest the presence of surface groups on the Pd rather than forming bare metal (*section 3.4*) [66, 67].

The variations seen in the XAFS can be isolated into 3 distinct regions during the reaction (Figure 7c). During the initial stages of the reaction (region **I**) there is a very slow increase in Pd(0) content however, as the onset potential has not yet been reached there is little distinct variation. The first CV performed in region **II** goes as high as 0.85 V which appears to indicate the onset of the reduction process from the hysteresis loop in Figure 3. Following on from this, there is a change in the gradient of the slope indicating an increase in the rate of Pd deposition, however further increases in the positive end of the potential window (up to 1.05 V) appears to have little further effect. Region **III** indicates the point at which bulk deposition was caused by the fixed potential indicated in Figure 7b. This produces a sharp increase in Pd(0) content where little further variation occurred.

3.2.3 Effect of interfacial potential on the deposition of Pd

The observations under potential control are in stark contrast to our previous work on the spontaneous deposition of $[PdCl_4]^{2-}$ measured using dispersive EXAFS. In the absence of an applied potential, the Pd concentration and oxidation state were seen to fluctuate over a number of hours [40, 43]. By introducing a fixed potential we have removed one of the possible degrees of freedom from the reaction therefore suppressing the oscillatory process. When the reactions are compared side by side (Figures 8) the fluctuations in edge step height in the presence (Figure 8a) and absence (Figure 8b) of potential control can be observed. The

reaction in Figure 8a was initiated by CV (Figure S4) before applying a fixed potential bias (0.40 V). Short potential pulses (0.85 V for 2, 5 or 10 s) were not found to influence the rate of growth. In contrast, in Figure 8b the reactant concentrations were higher (10 mM $PdCl_4$ | 20 mM Fc) and there was no control of the interfacial potential leading to dramatic fluctuations in concentration. (The variation in the edge shape in Figure 8b is due to the presence of Pd within the transmission detector on the ODE beamline at SOLEIL which lead to a non-linear transmission function, causing a slight distortion of the K-edge.) The potentiostatic system is able to exhibit global coupling across the interface which maintains electroneutrality within the electrolyte, stabilising the growth process [37]. Whereas the spontaneous system has no such constraint therefore enabling localised fluctuations in potential, disrupting the mass transport and leading to complex oscillations in the Pd deposition[43]. Whilst the effect of interfacial potential plays a pivotal role in the growth model both responses indicate a transition from Pd(II) to Pd(0) which, based on the chronoamperometric data discussed above, suggests the operation of a progressive nucleation model.

For the externally controlled reduction, the EXAFS response (Figure S5) showed a progression from Pd(II) to Pd(0) but did not indicate any clear variation in the bond lengths suggesting that the particles are formed by the coalescence of Pd(0) rather than the formation of intermediate species which contain both Pd-Pd and Pd-Cl bonds.

Figure 8 a and b

3.3 Size control of nanoparticle species

In the system described above, the products of the reaction are nanoparticulate, although there is little to control the shape and size of the products. To examine the shape of the clusters formed we performed a brief deposition sequence under potentiostatic conditions. The potentials applied were: 0.85 V (nucleation pulse for 0.5 s), followed by 0.4 V (slow growth for 20 s). TEM micrographs of the resultant nanoparticles are shown in Figure 9a. The absence of protecting groups has resulted in uneven particle shapes and sizes. The particles can be seen to be predominantly sub 10 nm, and lattice fringes can be seen indicating that the particles are crystalline rather than amorphous in nature, a full size distribution was not performed due to the non-spherical shape of the particles and the extent of aggregation observed. The liquid/liquid interface acts to partially stabilise the nanoparticles and it was observed that the deposits always remained at the interface rather than dropping to the bottom of the cell, in agreement with previous observations for the deposition of Pd [27].

Figures 9

To refine the deposition protocol we introduced 1 mM of citric acid to the aqueous phase to act as a stabilising ligand for the particle deposit. As the citric acid also acts as a weak reducing agent it was found that in conjunction with ferrocene the spontaneous reduction of Pd(II) to form nanoparticles was possible. There is no reaction between citric acid and Pd(II) in a single phase solution. In order to try and provide a good comparison with the particles formed in Figure 9a, the contact between the two phases prior to the application of potential was therefore kept to a minimum (~5 minutes). The same deposition protocol was used as for the deposition in the absence of citric acid (0.85 V, 0.5 s; 0.40 V, 20 s). In this case the

deposition results in the formation of smaller nanoparticles that are more uniform in shape and size (Figure 9b). The size of the nanoparticles formed was found to be 4.23 ± 0.88 nm.

3.4 Composition of the nanoparticle deposit examined by surface enhanced Raman spectroscopy (SERS)

The deposition reaction was also followed by in situ SERS spectroscopy. As with the XAFS measurements, a horizontal detector enabled measurement through the meniscus of the liquid/liquid interface to see any variations in species environment. Figure 10a indicates the Raman response recorded before and after deposition of the palladium nanoparticles. The increase in intensity seen in some of the Raman vibrational modes indicates that the bare nanoparticles assembled at the interface are able to provide some SERS enhancement. There have been previous reports in the literature that the presence of electrolyte in both solution phases is important when it comes to stabilising solid particles at the interface [68-70] and the response obtained here suggests that the organic electrolyte has assembled either on the surface of the nanoparticles or in close proximity. Figure 10b includes the Raman response for the TFT solvent and the organic electrolyte for comparison. As can be seen the blank sample matches well with that of the TFT solvent and the Pd deposition indicates the presence of peaks from the organic electrolyte BTPPATFPB, although there is some overlap with the solvent due to the similarity of the structures. Prior to the deposition of Pd, BTPPATFPB cannot be detected by Raman at a concentration of 10 mM. The spectra for BTPPACl and NaTFPB are shown if Figure S6 to identify the individual contributions from the anion and cation. Once the Pd has been deposited at the interface there is some enhancement of the solvent close to the nanoparticles and a significant enhancement of the organic electrolyte. Based on the work of Bell and co-workers [70] this would suggest that the electrolyte is acting as a modifier on the Pd nanoparticle surface following deposition.

This observation appears to match the variation between the nanoparticles and foil samples indicated in the XANES data (Figure 7d).

Figure 11

4. Conclusions

This work demonstrates the controlled electrodeposition of Pd nanoparticles at the liquid/liquid interface. Potentiostatic and potentiodynamic deposition is followed for the first time by in situ XAFS to give some idea of the distribution of Pd speciation, the oxidation state of the metal and the bonding of the reactants and products. LCF analysis suggests that there are no detectable stable intermediate species indicating the direct two electron reduction of $[PdCl_4]^{2-}$ to Pd^0 followed by the coalescence of Pd^0 atoms to form stable clusters. Potential control appears to eliminate the formation of long-lived pre-nucleation clusters involved in the oscillatory growth observed when the potential is not constrained. Applied potentials above or below (0.30 V or 0.40 V) the reduction potential (0.39 V) did not show any significant variation in growth rate suggesting that the reaction relies on the application of a significant overpotential (~0.46 V) for initiation. Although it is possible to initiate the nucleation process electrochemically, subsequent control of the rate of reaction by applied potential is limited within the accessible potential window. Following the initial nucleation the reaction may be autocatalytic, i.e. progressive, proceeding at a slow rate unless the reaction is held at 0.85 V to drive rapid deposition. Once formed, the particles undergo surface modification to enable their stability at the liquid/liquid interface either through the adsorption of the organic cation or citric acid molecules.

5. Acknowledgements

We thank Diamond Light Source for the award of beamtime on B18 under proposal number SP13953 and Synchrotron SOLEIL for the award of beamtime on ROCK under proposal number 20151221 and ODE under proposal 20141060. The work on ROCK was supported by a public grant overseen by the French National Research Agency (ANR) as part of the 'Investissements d'Avenir' program (reference: ANR-10-EQPX-45). SLMS and RAWD acknowledge financial support for this project from the EPSRC through an EPSRC-NSF Materials World Network grant (EP/H047786/1) and RAWD acknowledges further support from EPSRC grant (EP/K007033/1). AU acknowledges grant (No. 16K06958) from the Ministry of Education, Culture, Sports, Science and Technology, Japan. The authors would also like to thank Van-Thai Pham and Lucie Nataf for their assistance during the beamtime on ODE.

6. References

[1] J. Turkevich, P.C. Stevenson, J. Hillier, A Study of the Nucleation and Growth Processes in the Synthesis of Colloidal Gold, Discussions of the Faraday Society, (1951) 55-75.
[2] P.C. Lee, D. Meisel, Adsorption and Surface-Enhanced Raman of Dyes on Silver and Gold Sols, Journal of Physical Chemistry, 86 (1982) 3391-3395.
[3] M. Brust, M. Walker, D. Bethell, D.J. Schiffrin, R. Whyman, Synthesis of Thiol-Derivatized Gold Nanoparticles in a 2-Phase Liquid-Liquid System, Journal of the Chemical Society-Chemical Communications, (1994) 801-802.
[4] C.M. Volkle, D. Gebauer, H. Colfen, High-resolution insights into the early stages of silver nucleation and growth, Faraday Discussions, 179 (2015) 59-77.
[5] P. Raiteri, J.D. Gale, Water Is the Key to Nonclassical Nucleation of Amorphous Calcium Carbonate, Journal of the American Chemical Society, 132 (2010) 17623-17634.
[6] A.S. Myerson, Concluding remarks, Faraday Discussions, 179 (2015) 543-547.
[7] X.L. Chen, J. Schroder, S. Hauschild, S. Rosenfeldt, M. Dulle, S. Forster, Simultaneous SAXS/WAXS/UV-Vis Study of the Nucleation and Growth of Nanoparticles: A Test of Classical Nucleation Theory, Langmuir, 31 (2015) 11678-11691.
[8] F. Kettemann, M. Wuithschick, G. Caputo, R. Kraehnert, N. Pinna, K. Rademann, J. Polte, Reliable palladium nanoparticle syntheses in aqueous solution: the importance of understanding precursor chemistry and growth mechanism, Crystengcomm, 17 (2015) 1865-1870.
[9] Y.G. Sun, Y. Ren, In Situ Synchrotron X-Ray Techniques for Real-Time Probing of Colloidal Nanoparticle Synthesis, Particle & Particle Systems Characterization, 30 (2013) 399-419.
[10] J. Polte, T.T. Ahner, F. Delissen, S. Sokolov, F. Emmerling, A.F. Thunemann, R. Kraehnert, Mechanism of Gold Nanoparticle Formation in the Classical Citrate Synthesis Method Derived from Coupled In Situ XANES and SAXS Evaluation, Journal of the American Chemical Society, 132 (2010) 1296-1301.

[11] J. Ohyama, K. Teramura, Y. Higuchi, T. Shishido, Y. Hitomi, K. Kato, H. Tanida, T. Uruga, T. Tanaka, In Situ Observation of Nucleation and Growth Process of Gold Nanoparticles by Quick XAFS Spectroscopy, Chemphyschem, 12 (2011) 127-131.
[12] T. Yao, Z.H. Sun, Y.Y. Li, Z.Y. Pan, H. Wei, Y. Xie, M. Nomura, Y. Niwa, W.S. Yan, Z.Y. Wu, Y. Jiang, Q.H. Liu, S.Q. Wei, Insights into Initial Kinetic Nucleation of Gold Nanocrystals, Journal of the American Chemical Society, 132 (2010) 7696-7701.
[13] C. Nayak, D. Bhattacharyya, S.N. Jha, N.K. Sahoo, Growth of block copolymer stabilized metal nanoparticles probed simultaneously by in situ XAS and UV-Vis spectroscopy, Journal of Synchrotron Radiation, 23 (2016) 293-303.
[14] D. Gebauer, A. Volkel, H. Colfen, Stable Prenucleation Calcium Carbonate Clusters, Science, 322 (2008) 1819-1822.
[15] Y. Mikhlin, A. Karacharov, M. Likhatski, T. Podlipskaya, Y. Zubavichus, A. Veligzhanin, V. Zaikovski, Submicrometer intermediates in the citrate synthesis of gold nanoparticles: New insights into the nucleation and crystal growth mechanisms, Journal of Colloid and Interface Science, 362 (2011) 330-336.
[16] V.C. Diculescu, A.M. Chiorcea-Paquim, O. Corduneanu, A.M. Oliveira-Brett, Palladium nanoparticles and nanowires deposited electrochemically: AFM and electrochemical characterization, Journal of Solid State Electrochemistry, 11 (2007) 887-898.
[17] L.H. Mendoza-Huizar, D. Garrido-Marquez, C.H. Rios-Reyes, M. Rivera, E. Garcia-Sanchez, C. Galan-Vidal, A Kinetic and AFM Study of the Electrodeposition of Palladium Nanoclusters onto Highly Oriented Pyrolytic Graphite (HOPG), Journal of Cluster Science, 26 (2015) 337-346.
[18] J. Ustarroz, X.X. Ke, A. Hubin, S. Bals, H. Terryn, New Insights into the Early Stages of Nanoparticle Electrodeposition, Journal of Physical Chemistry C, 116 (2012) 2322-2329.
[19] S.C.S. Lai, R.A. Lazenby, P.M. Kirkman, P.R. Unwin, Nucleation, aggregative growth and detachment of metal nanoparticles during electrodeposition at electrode surfaces, Chemical Science, 6 (2015) 1126-1138.
[20] M. Guainazzi, G. Silvestri, G. Serravalle, Electrochemical Metallization at Liquid-Liquid Interfaces of Non-Miscible Electrolytic Solutions, Journal of the Chemical Society-Chemical Communications, (1975) 200-201.
[21] Y.F. Cheng, D.J. Schiffrin, Electrodeposition of Metallic Gold Clusters at the Water/1,2-dichloroethane Interface, Journal of the Chemical Society-Faraday Transactions, 92 (1996) 3865-3871.
[22] A. Uehara, T. Hashimoto, R.A.W. Dryfe, Au Electrodeposition at the Liquid-Liquid Interface: Mechanistic Aspects, Electrochimica Acta, 118 (2014) 26-32.
[23] C. Johans, J. Clohessy, S. Fantini, K. Kontturi, V.J. Cunnane, Electrosynthesis of polyphenylpyrrole coated silver particles at a liquid-liquid interface, Electrochemistry Communications, 4 (2002) 227-230.
[24] J.D. Guo, T. Tokimoto, R. Othman, P.R. Unwin, Formation of Mesoscopic Silver Particles at Micro- and Nano-Liquid/Liquid Interfaces, Electrochemistry Communications, 5 (2003) 1005-1010.
[25] A. Trojanek, J. Langmaier, Z. Samec, Random Nucleation and Growth of Pt Nanoparticles at the Polarised Interface Between Two Immiscible Electrolyte Solutions, Journal of Electroanalytical Chemistry, 599 (2007) 160-166.
[26] M. Platt, R.A.W. Dryfe, E.P.L. Roberts, Structural and Electrochemical Characterisation of Pt and Pd Nanoparticles Electrodeposited at the Liquid/Liquid Interface, Electrochimica Acta, 49 (2004) 3937-3945.
[27] M. Platt, R.A.W. Dryfe, Structural and electrochemical characterisation of Pt and Pd nanoparticles electrodeposited at the liquid/liquid interface: Part 2, Physical Chemistry Chemical Physics, 7 (2005) 1807-1814.
[28] C. Johans, R. Lahtinen, K. Kontturi, D.J. Schiffrin, Nucleation at liquid vertical bar liquid interfaces: electrodeposition without electrodes, Journal of Electroanalytical Chemistry, 488 (2000) 99-109.
[29] R.A.W. Dryfe, A. Uehara, S.G. Booth, Metal Deposition at the Liquid-Liquid Interface, Chemical Record, 14 (2014) 1013-1023.

[30] Y. Gründer, H.L.T. Ho, J.F.W. Mosselmans, S.L.M. Schroeder, R.A.W. Dryfe, Inhibited and Enhanced Nucleation of Gold Nanoparticles at the Water Vertical Bar 1,2-dichloroethane Interface, Physical Chemistry Chemical Physics, 13 (2011) 15681-15689.
[31] S.G. Booth, A. Uehara, S.Y. Chang, J.F.W. Mosselmans, S.L.M. Schroeder, R.A.W. Dryfe, Gold Deposition at a Free-Standing Liquid/Liquid Interface: Evidence for the Formation of Au(I) by Microfocus X-ray Spectroscopy (mu XRF and mu XAFS) and Cyclic Voltammetry, Journal of Physical Chemistry C, 119 (2015) 16785-16792.
[32] B.P. Binks, S.O. Lumsdon, Influence of Particle Wettability on the Type and Stability of Surfactant-Free Emulsions, Langmuir, 16 (2000) 8622-8631.
[33] B.P. Binks, J.H. Clint, Solid wettability from surface energy components: Relevance to pickering emulsions, Langmuir, 18 (2002) 1270-1273.
[34] D. Kashchiev, G.M. van Rosmalen, Review: Nucleation in solutions revisited, Cryst. Res. Technol., 38 (2003) 555-574.
[35] D. Erdemir, A.Y. Lee, A.S. Myerson, Nucleation of Crystals from Solution: Classical and Two-Step Models, Accounts of Chemical Research, 42 (2009) 621-629.
[36] J.V. Macpherson, P.R. Unwin, OSCILLATORY DISSOLUTION OF AN IONIC SINGLE-CRYSTAL SURFACE OBSERVED WITH THE SCANNING ELECTROCHEMICAL MICROSCOPE, Journal of Physical Chemistry, 98 (1994) 11764-11770.
[37] M.T.M. Koper, Non-linear phenomena in electrochemical systems, Journal of the Chemical Society-Faraday Transactions, 94 (1998) 1369-1378.
[38] Y. Kimura, H. Niinomi, K. Tsukamoto, J.M. Garcia-Ruiz, In Situ Live Observation of Nucleation and Dissolution of Sodium Chlorate Nanoparticles by Transmission Electron Microscopy, Journal of the American Chemical Society, 136 (2014) 1762-1765.
[39] M.H. Nielsen, D.S. Li, H.Z. Zhang, S. Aloni, T.Y.J. Han, C. Frandsen, J. Seto, J.F. Banfield, H. Colfen, J.J. De Yoreo, Investigating Processes of Nanocrystal Formation and Transformation via Liquid Cell TEM, Microscopy and Microanalysis, 20 (2014) 425-436.
[40] S.Y. Chang, Y. Grunder, S.G. Booth, L.B. Molleta, A. Uehara, J.F.W. Mosselmans, G. Cibin, V.T. Pham, L. Nataf, R.A.W. Dryfe, S.L.M. Schroeder, Detection and characterisation of sub-critical nuclei during reactive Pd metal nucleation by X-ray absorption spectroscopy, Crystengcomm, 18 (2016) 674-682.
[41] R.M. Lahtinen, D.J. Fermin, H. Jensen, K. Kontturi, H.H. Girault, Two-phase photocatalysis mediated by electrochemically generated Pd nanoparticles, Electrochemistry Communications, 2 (2000) 230-234.
[42] R.A.W. Dryfe, A.O. Simm, B. Kralj, Electroless deposition of palladium at bare and templated liquid/liquid interfaces, Journal of the American Chemical Society, 125 (2003) 13014-13015.
[43] S.Y. Chang, S.G. Booth, A. Uehara, J.F.W. Mosselmans, G. Cibin, V.T. Pham, L. Nataf, R.A.W. Dryfe, S.L.M. Schreoder, Energy dispersive-EXAFS of Pd nucleation at a liquid/liquid interface, Journal of Physics: Conference Series, 712 (2016) 012058.
[44] D.J. Fermin, H.D. Duong, Z.F. Ding, P.F. Brevet, H.H. Girault, Photoinduced Electron Transfer at Liquid/Liquid Interfaces - Part II. A Study of the Electron Transfer and Recombination Dynamics by Intensity Modulated Photocurrent Spectroscopy (IMPS), Physical Chemistry Chemical Physics, 1 (1999) 1461-1467.
[45] P. Vanysek, V. Novak, Liquid/liquid Electrochemistry in Electroanalysis: Fundamentals Revisited, ECS Trans., 19 (2009) 55-63.
[46] A. Uehara, S.G. Booth, S.Y. Chang, S.L.M. Schroeder, T. Imai, T. Hashimoto, J.F.W. Mosselmans, R.A.W. Dryfe, Electrochemical Insight into the Brust-Schiffrin Synthesis of Au Nanoparticles, Journal of the American Chemical Society, 137 (2015) 15135-15144.
[47] A.J. Dent, G. Cibin, S. Ramos, A.D. Smith, S.M. Scott, L. Varandas, M.R. Pearson, N.A. Krumpa, C.P. Jones, P.E. Robbins, B18: A core XAS spectroscopy beamline for Diamond, 14th International Conference on X-Ray Absorption Fine Structure (XAFS14), Iop Publishing Ltd, Camerino, ITALY, 2009.
[48] V. Briois, C. La Fontaine, S. Belin, L. Barthe, T. Moreno, V. Pinty, A. Carcy, R. Girardot, E. Fonda, ROCK: the new Quick-EXAFS beamline at SOLEIL, Journal of Physics: Conference Series, 712 (2016) 012149.

[49] F. Baudelet, Q. Kong, L. Nataf, J.D. Cafun, A. Congeduti, A. Monza, S. Chagnot, J.P. Itie, ODE: a new beam line for high-pressure XAS and XMCD studies at SOLEIL, High Pressure Res., 31 (2011) 136-139.
[50] B. Ravel, M. Newville, Athena, Artemis, Hephaestus: Data Analysis for X-ray Absorption Spectroscopy using IFEFFIT, Journal of Synchrotron Radiation, 12 (2005) 537-541.
[51] P. Vanýsek, Electrochemical Series, in: W.M. Heynes (Ed.) CRC Handbook of Chemistry and Physics, CRC Press, Boca Raton, 2016, pp. 78-84.
[52] C. Johans, P. Liljeroth, K.S. Kontturi, Electrodeposition at Polarisable Liquid Vertical Bar Liquid Interfaces: The Role of Interfacial Tension on Nucleation Kinetics, Physical Chemistry Chemical Physics, 4 (2002) 1067-1071.
[53] M.A. Mendez, R. Partovi-Nia, I. Hatay, B. Su, P.Y. Ge, A. Olaya, N. Younan, M. Hojeij, H.H. Girault, Molecular electrocatalysis at soft interfaces, Physical Chemistry Chemical Physics, 12 (2010) 15163-15171.
[54] V.J. Cunnane, G. Geblewicz, D.J. Schiffrin, ELECTRON AND ION TRANSFER POTENTIALS OF FERROCENE AND DERIVATIVES AT A LIQUID-LIQUID INTERFACE, Electrochimica Acta, 40 (1995) 3005-3014.
[55] I. Hatay, B. Su, F. Li, M.A. Mendez, T. Khoury, C.P. Gros, J.M. Barbe, M. Ersoz, Z. Samec, H.H. Girault, Proton-Coupled Oxygen Reduction at Liquid-Liquid Interfaces Catalyzed by Cobalt Porphine, Journal of the American Chemical Society, 131 (2009) 13453-13459.
[56] C. Johans, K. Kontturi, D.J. Schiffrin, Nucleation at liquid vertical bar liquid interfaces: galvanostatic study, Journal of Electroanalytical Chemistry, 526 (2002) 29-35.
[57] M. Platt, R.A.W. Dryfe, E.P.L. Roberts, Electrodeposition of palladium nanoparticles at the liquid-liquid interface using porous alumina templates, Electrochimica Acta, 48 (2003) 3037-3046.
[58] J.J. Nieminen, I. Hatay, P.Y. Ge, M.A. Mendez, L. Murtomaki, H.H. Girault, Hydrogen evolution catalyzed by electrodeposited nanoparticles at the liquid/liquid interface, Chemical Communications, 47 (2011) 5548-5550.
[59] B. Scharifker, G. Hills, THEORETICAL AND EXPERIMENTAL STUDIES OF MULTIPLE NUCLEATION, Electrochimica Acta, 28 (1983) 879-889.
[60] O. Brylev, L. Roue, D. Belanger, Rhodium electrodeposition on pyrolytic graphite electrode: Analysis of chronoamperometric curves, Journal of Electroanalytical Chemistry, 581 (2005) 22-30.
[61] T. Nguyen, M.J. Carmezim, M.F. Montemor, Current transient and in situ AFM studies of initial growth stages of electrochemically deposited nickel cobalt hydroxide nanosheet films, Physical Chemistry Chemical Physics, 18 (2016) 12368-12374.
[62] F. Li, M. Edwards, J.D. Guo, P.R. Unwin, Silver Particle Nucleation and Growth at Liquid/Liquid Interfaces: A Scanning Electrochemical Microscopy Approach, Journal of Physical Chemistry C, 113 (2009) 3553-3565.
[63] A. Uehara, S.Y. Chang, S.G. Booth, S.L.M. Schroeder, J.F.W. Mosselmans, R.A.W. Dryfe, Redox and Ligand Exchange during the Reaction of Tetrachloroaurate with Hexacyanoferrate(II) at a Liquid-Liquid Interface: Voltammetry and X-ray Absorption Fine-Structure Studies, Electrochimica Acta, 190 (2016) 997-1006.
[64] J.E. Muller, O. Jepsen, O.K. Andersen, J.W. Wilkins, SYSTEMATIC STRUCTURE IN K-EDGE PHOTOABSORPTION SPECTRA OF 4D TRANSITION-METALS - THEORY, Physical Review Letters, 40 (1978) 720-722.
[65] C.M. Lin, T.L. Hung, Y.H. Huang, K.T. Wu, M.T. Tang, C.H. Lee, C.T. Chen, Y.Y. Chen, Size-dependent lattice structure of palladium studied by x-ray absorption spectroscopy, Physical Review B, 75 (2007) 6.
[66] J. Nilsson, P.-A. Carlsson, H. Gronbeck, M. Skoglundh, First Principles Calculations of Palladium Nanoparticle XANES Spectra, Top. Catal., (2016) 1-6.
[67] A.L. Bugaev, A.A. Guda, K.A. Lomachenko, L.A. Bugaev, A.V. Soldatov, Pd hydride and carbide studied by means of Pd K-edge X-ray absorption near-edge structure analysis, Bulletin of the Russian Academy of Sciences: Physics, 79 (2015) 1180-1185.
[68] M.K. Bera, H. Chan, D.F. Moyano, H. Yu, S. Tatur, D. Amoanu, W. Bu, V.M. Rotello, M. Meron, P. Kral, B.H. Lin, M.L. Schlossman, Interfacial Localization and Voltage-Tunable Arrays of Charged Nanoparticles, Nano Letters, 14 (2014) 6816-6822.

[69] A.N.J. Rodgers, M. Velicky, R.A.W. Dryfe, Electrostatic Stabilization of Graphene in Organic Dispersions, Langmuir, 31 (2015) 13068-13076.
[70] Y. Xu, M.P. Konrad, W.W.Y. Lee, Z. Ye, S.E.J. Bell, A Method for Promoting Assembly of Metallic and Nonmetallic Nanoparticles into Interfacial Monolayer Films, Nano Letters, 16 (2016) 5255-5260.

Figures

Figure 1

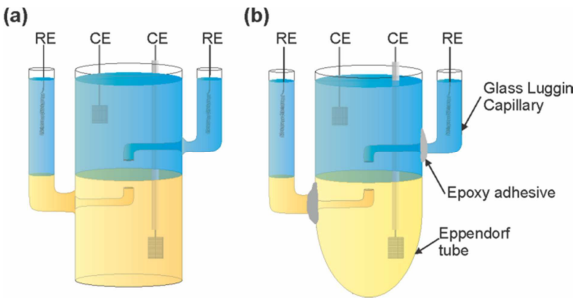

Figure 1. Schematic illustration of the 4-electrode electrochemical cells used in this study. The aqueous phase is coloured blue and the organic phase is coloured in yellow. The abbreviations CE and RE refer to the counter electrodes and reference electrodes, respectively. Cell A is constructed out of glass whilst cell B consists of a polypropylene Eppendorf tube connected to glass capillaries by epoxy adhesive.

Figure 2

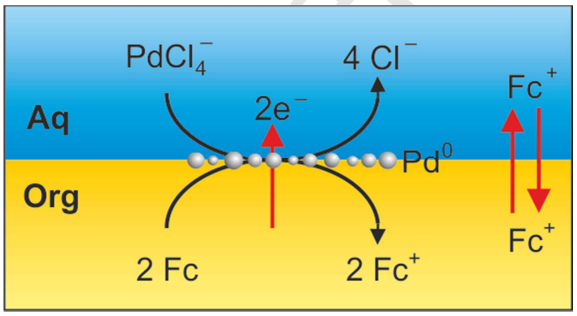

Figure 2. Schematic illustration of the electron transfer process occurring at the liquid/liquid interface

Figure 3

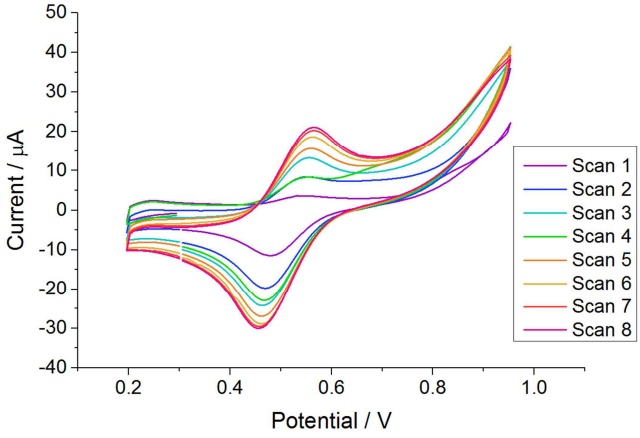

Figure 3. Cyclic voltammograms at a water|TFT interface using a standard glass 4-electrode electrochemical cell. The aqueous phase contained 1 mM $[PdCl_4]^{2-}$ and the organic phase contained 4 mM Fc. The scan rate was 50 mV s^{-1}

Figure 4

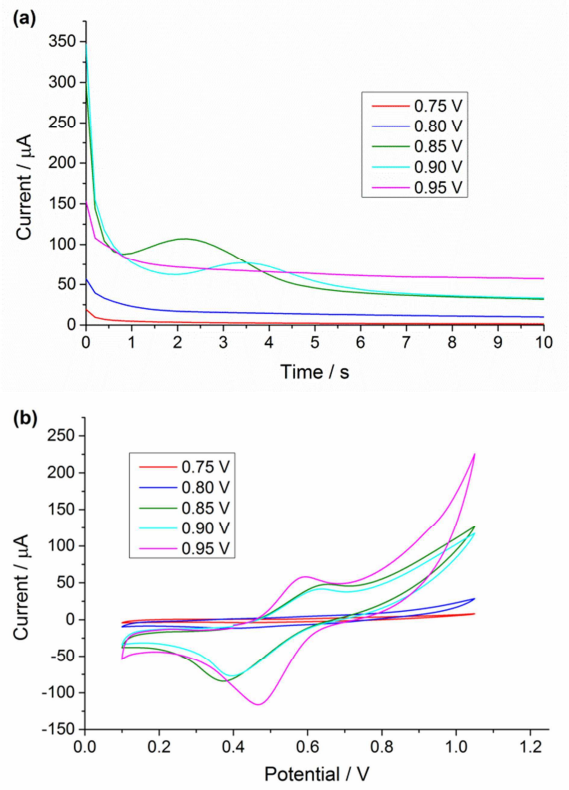

Figure 4. (a) Current transients at a freshly prepared water|TFT interface, 1 mM $[PdCl_4]^{2-}_{(aq)}$|10 mM $Fc_{(org)}$. (b) Cyclic voltammogram of the water|TFT interface directly following the application of a fixed potential for 180 s (Figure 4a). Scan rate is 100 mV s^{-1}.

Figure 5

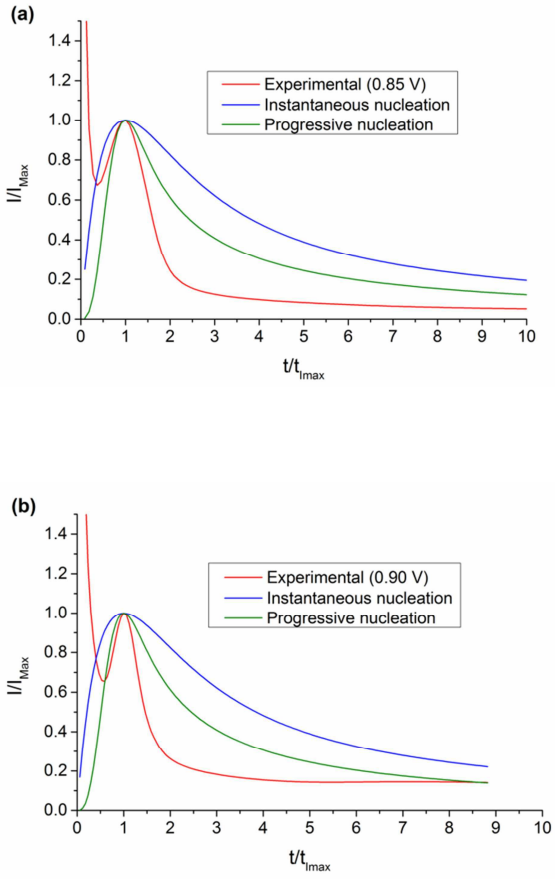

Figure 5. Comparison between experimental responses at the liquid/liquid interface and the Scharifker-Hills models for instantaneous and progressive nucleation showing a similar response at both (a) 0.85 V and (b) 0.90 V

Figure 6

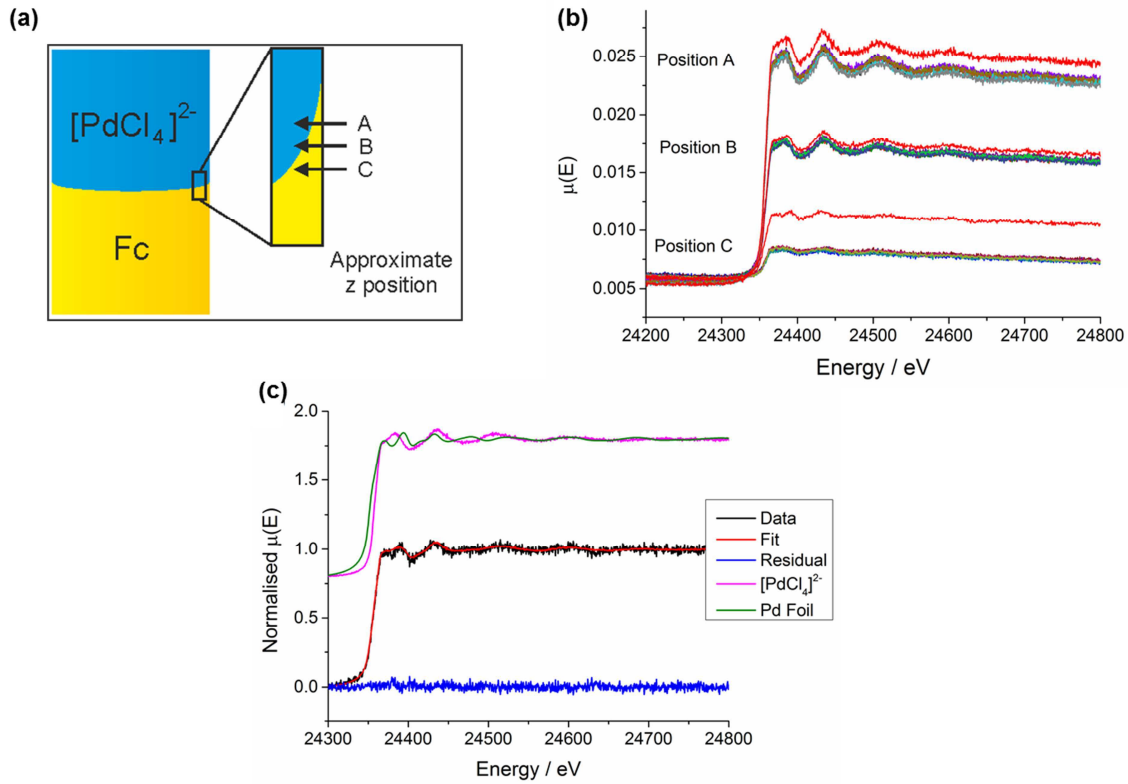

Figure 6. (a) Schematic indicating how the variation in sample position relates to variation in the XAFS response. (b) XAFS fluorescence data collected at the Diamond Light Source over a period of 3.5 hours at a fixed potential of 0.3 V and then 0.4 V (coloured scans) and following cyclic voltammetry (red scans). Positions A, B and C correspond to different heights through the liquid/liquid interface, separated by 500 μm. (c) LCF to standards of the XANES region of the red spectrum at position C (Figure 6b) i.e. following deposition. The plot contains the data and fit alongside the residual signal, and offset fitting components.

Figure 7

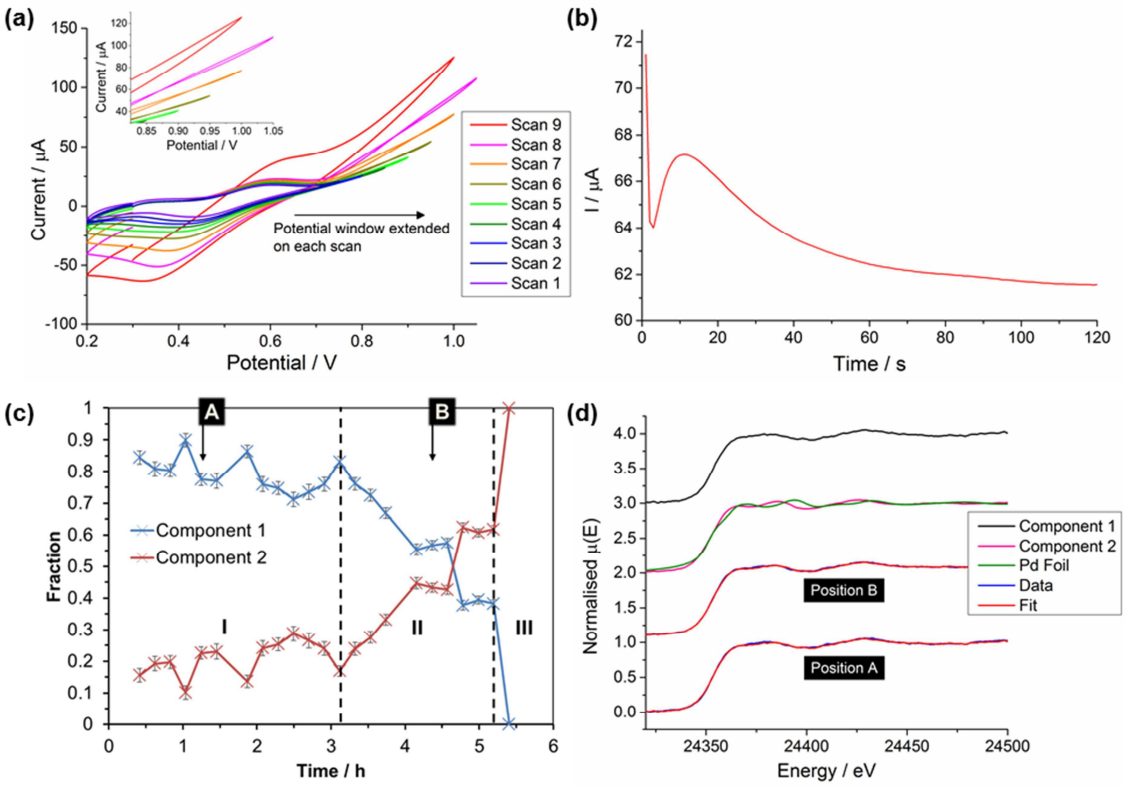

Figure 7. (a) Cyclic voltammograms recorded at the water|TFT interface. The aqueous phase contained 5 mM $[PdCl_4]^{2-}$ and the organic phase contained 5 mM Fc. Starting at 0.7 V the positive limit of the potential window was extended by 0.05 V with each scan up to 1.05 V. The positive region of the potential window is enhanced in the figure inset showing that scans 6, 7 and 8 all produced a hysteresis loop at positive potentials. Scan 9 appears to have reached bulk growth as there is no hysteresis loop. The scan rate was 25 mV s^{-1}. (b) Constant potential current response for an applied potential of 0.85 V (120 s). The chronoamperometry was performed on the same cell shortly after CV scan 9 (a). (c) Concentration profile determined by LCF analysis of the Pd K-edge XANES data, collected on the ROCK beamline at SOLEIL, during cycling as indicated in (a). The region marked by **I** corresponds

to the scans collected prior to the application of potential and during scans 1-3. Region **II** corresponds to the variation seen during scans 4-9. Region **III** indicates the reactant composition following the chronoamperometric pulse shown in (b). (d) Example data and corresponding LCF for positions A and B marked in (c). Component 2 (Pd deposit) is compared directly to Pd foil and the initial $[PdCl_4]^{2-}$ spectrum is provided for comparison.

Figure 8

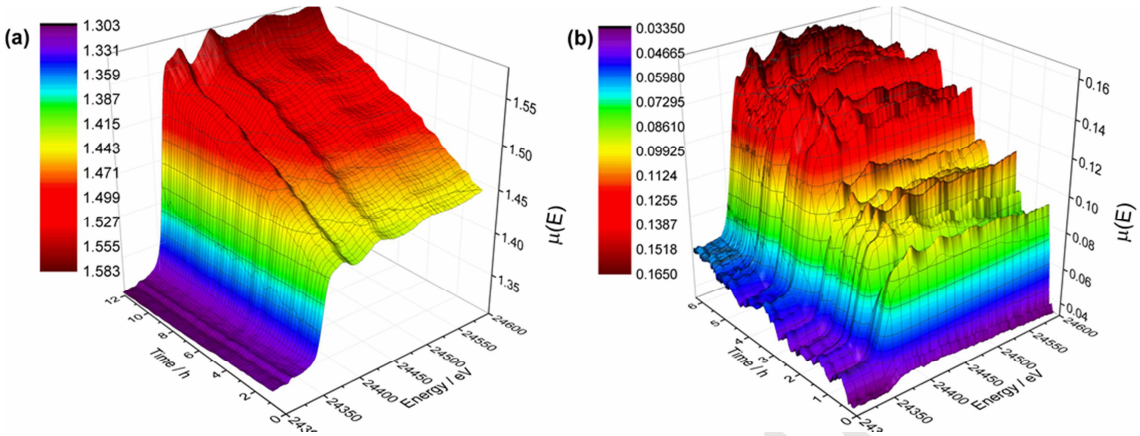

Figure 8. (a) Pd K-edge XANES data (QEXAFS on the ROCK beamline at SOLEIL) following the electrochemically driven onset of nucleation. The shape of the K-edge can be seen to change on increasing scan number as the reaction proceeds from Pd(II) to Pd(0). The aqueous phase contained 5 mM $[PdCl_4]^{2-}$ and the organic phase contained 5 mM Fc. (b) Pd K-edge XANES data (dispersive EXAFS on the ODE beamline at SOLEIL) of the spontaneous nucleation at the liquid/liquid interface in the absence of any external control of the interfacial potential. The aqueous phase contained 10 mM $[PdCl_4]^{2-}$ and the organic phase contained 20 mM Fc.

Figure 9

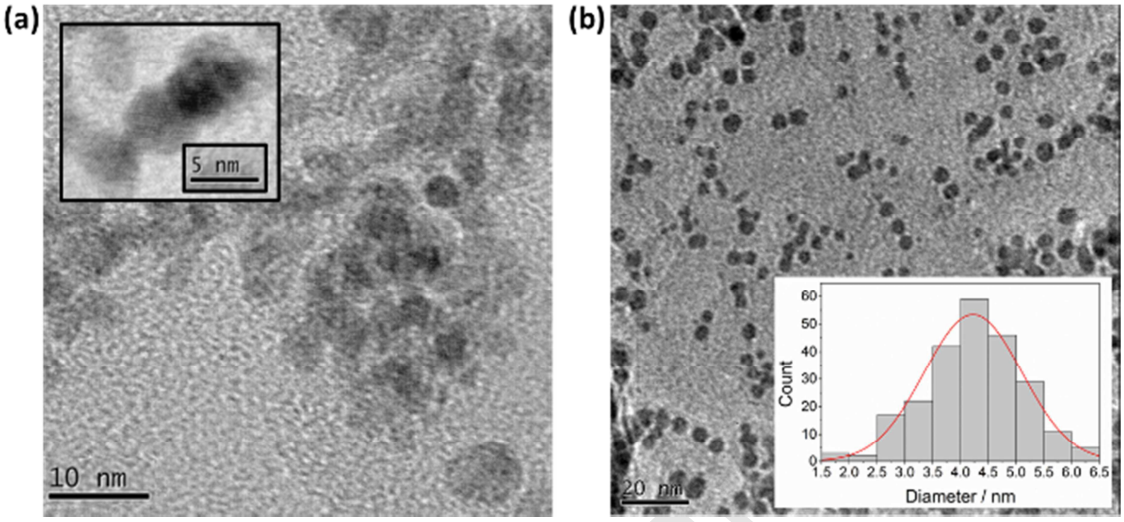

Figure 9. TEM micrographs of the Pd deposition products. These nanoparticles were formed following the deposition sequence: 0.85 V, 0.5 s; 0.40 V, 20 s. (a) In the absence of citric acid (b) in the presence of citric acid. The inset in (b) shows the particle size distribution histogram.

Figure 10

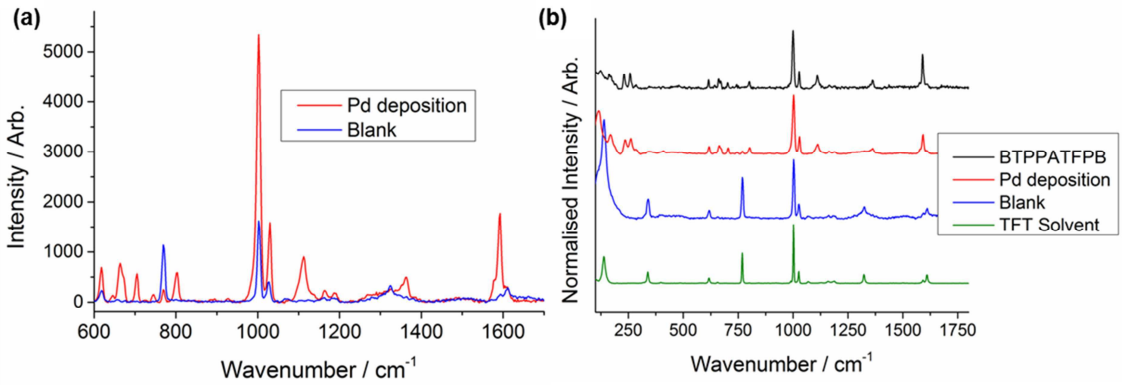

Figure 10. (a) Variation in Raman response at the liquid/liquid interface before and after the deposition of Pd nanoparticles. (b) The Raman responses from (a) alongside measurements of TFT and solid BTPPATFPB. Each spectrum was normalized to the response at 1000 cm^{-1} to enable clear comparison of the wavebands.